Powder Technology 437 (2024) 119538

Contents lists available at ScienceDirect

Powder Technology

journal homepage: www.journals.elsevier.com/powder-technology

Numerical investigation of particle re-entrainment mechanism and its suppression strategy in the high-temperature electrostatic precipitator

Yongmin Shi [a], Chao Li [a,*], Mengxiang Fang [a], Jianmeng Cen [a], Qinhui Wang [a], Keping Yan [b]

[a] State Key Lab of Clean Energy Utilization, Zhejiang University, Hangzhou 310027, China
[b] Coll Chem & Biol Engn, Inst Ind Ecol & Environm, Zhejiang University, Hangzhou 310028, China

HIGHLIGHTS

- A modified high-temperature ESP model involving particle re-entrainment was developed
- The effect of temperature on the electric and flow field was investigated numerically.
- The effect of temperature on the particle re-entrainment was evaluated.
- The effectiveness of different types of collection electrodes in reducing particle re-entrainment was evaluated.

GRAPHICAL ABSTRACT

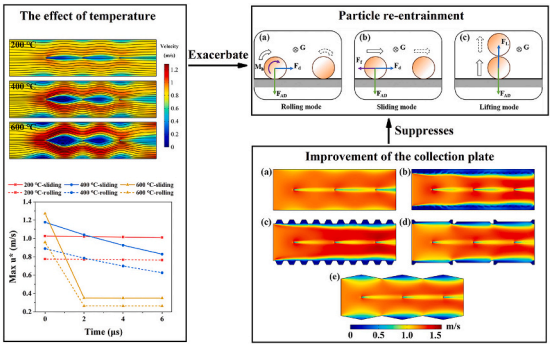

ARTICLE INFO

Keywords:
Electrostatic precipitator
Simulation
High temperature
Particle re-entrainment

ABSTRACT

An integrated model was developed to investigate the effect of temperature on the particle re-entrainment in a high-temperature electrostatic precipitator (ESP). The numerical model considered the electric field, flow field, particle migration, and particle re-suspension due to the rupture of static equilibrium. The electric and flow field distributions at different temperatures were investigated. The minimum critical shear velocity needed to detach high-temperature deposited particles from the plate surface was calculated and discussed. On these basis, five types of ESPs with collection plates of different configurations were compared. The results show that high temperatures will exacerbate particle re-entrainment caused by airflow scouring and electrostatic lifting by enhancing the ionic wind and reducing particle resistivity. The hole-type plate may be a better plate form to reduce re-entrainment in the high-temperature ESPs, as it creates a low velocity, low electric field region in the near-plate region.

1. Introduction

High-temperature particle removal technology plays an essential role in many industries involving high temperature gases [1]. For instance, in integrated gasification combined cycle (IGCC) and pressurized fluidized bed combustion (PFBC), the effective removal of particles in high temperature gases is essential in order to protect downstream components from contamination or to improve the quality

* Corresponding author.
E-mail address: lichaozjuer@zju.edu.cn (C. Li).

https://doi.org/10.1016/j.powtec.2024.119538
Received 19 December 2023; Received in revised form 12 February 2024; Accepted 15 February 2024
Available online 17 February 2024

of coal chemical products [2,3]. The following high-temperature particle removal technologies are currently available: granular bed filters, ceramic filters, cyclone separators and electrostatic precipitators (ESPs) [4–7]. ESPs have been extensively applied to reduce particle concentration from industrial flue gases at low temperatures (<300 °C) due to their low operating costs, high collection efficiency and the fact that they can be used to treat complex flue gases and particulate matter [8]. Therefore, high-temperature ESPs are considered as a potential high-temperature (>350 °C) gas cleaning method [9].

Early researchers usually limited the focus of high-temperature ESP to high temperature discharge characteristics. Thomas et al. [10] and Bush et al. [11] mainly investigated the impact of high pressure and high temperature on corona discharge characteristics and did not perform electrostatic precipitation experiments. In recent years, a large number of more comprehensive high-temperature ESP experiments incorporating corona discharge and electrostatic precipitation have been conducted. Xiao et al. [12,13] performed corona discharge experiments and electrostatic precipitation experiments at temperatures ranging from 350 °C to 700 °C and obtained particle collection efficiency >99.6% at high temperatures. Bürger et al. [14,15] evaluated the discharge characteristics and dust removal characteristics of a high temperature ESP under two different polarity power supplies. However, some studies have shown that the decrease in breakdown voltage of the ESP at high temperatures leads to a decrease in the maximum collection efficiency, thus limiting the performance of high-temperature ESPs [16–18]. ESP structural optimization, power supply polarity adjustment, gas media conditioning, etc. have been proposed to solve this problem [19,20]. Moreover, the re-entrainment effect of high-temperature particles is an important factor limiting the further improvement of the performance of high-temperature ESPs. In ESPs, collected particles are adsorbed on the collecting plate by adhesion forces, whereas fluid forces tend to move the particles away from the plate surface. In other words, it is possible for the collected particles to return to the gas stream (known as re-entrainment) [21]. Zheng et al. [22] conducted dust removal experiments in a closed-loop ESP system, and they suggested that there exists a limiting collection efficiency for ESPs due to the balance between electrostatic capture and particle re-entrainment. Our previous research also found that the collection efficiency gradually tends to a stable value below 100% as the applied voltage increases, and this value decreases with increasing temperature [20]. Similar phenomena have also been found in other studies [12]. Therefore, it is crucial to understand the particle re-entrainment effect in high-temperature ESPs to further improve the performance of high-temperature ESPs.

Current research on particle re-entrainment mainly focuses on analyzing the flow field and the behavior of the deposited particles. The flow field of an ESP is often being called the electrohydrodynamic flow (EHD) which is formed by the coupling of the ionic wind and the main airflow. In the migration region of a corona electric field, charged particles migrate by the action of the electric field and exchange momentum upon collision with neutral molecules. The directional motion of these particles forms the ionic wind. Recently, the particle image velocimetry (PIV) method has been an effective experimental tool to study the flow inside an ESP and to track the particle motion. Podlinski et al. [23,24] visualized the EHD flow inside spike-plate and wire-plate ESPs using the PIV technique. Ning et al. [25] investigated the flow field of a wide-type ESP and discussed the effect of the number and arrangement of discharge electrodes. Yan et al. [26] investigated the EHD flow inside an ESP with barbed tubular electrodes and showed that the particle re-entrainment was closely related to the phenomena of “vacuum vortex obstruction” and “high-velocity flow driven deposition”. Krupa et al. [27] gave the PIV measurements of the velocity field of the EHD flow during the back corona. Yuan et al. [28] successfully visualized and analyzed re-entrained particles using the PIV method. However, the exterior of high temperature ESPs usually need to be encased in thick insulation and are not suitable for direct measurements with PIV. Therefore, numerical simulation, which has been widely used to study flow field distribution and particle behavior, can be a more appropriate research tool [29]. Many numerical simulation studies have been conducted to explore the effects of factors such as the structure of the ESP, voltage, flow rate, etc. on the flow field and particle behavior [30–33]. However, the above experimental and simulation studies have been conducted at room temperature and there exists a lack of researches on high-temperature ESPs. Furthermore, the analysis of the behavior of the deposited particles is also lacking.

In this study, a comprehensive numerical model of an ESP incorporating a particle re-entrainment model was developed by using COMSOL Multiphysics. The effect of temperature on the EHD flow of the ESP was investigated in the temperature range of 200–600 °C. The electrostatic force and contact pull-off force acting on the deposited particles were investigated. The minimum critical shear velocities needed to separate charged particles from the collecting plate at various temperatures were evaluated. On this basis, the flow field and electric field distributions of ESPs with five different structures of collection electrodes were compared to explore the optimal collection electrodes for suppressing re-entrainment in high-temperature ESPs.

2. Numerical method

In an ESP, dust particles become charged when they collide with ions. Then the charged particles migrate towards the collecting plate due to the electric field, and eventually get adsorbed onto the plate due to the adhesion force. Therefore, the ESP model in this work coupled the process of corona discharge, gas flow, particle charging and migration, and particle adhesion.

2.1. Corona field

The governing equations for the electric field consisted of the Poisson equation and the current continuity equation, expressed as follows:

Poisson equation:

$$\nabla^2\varphi = -\frac{\rho_i}{\varepsilon_0} \tag{1}$$

Current continuity equation:

$$J = \rho_i(k_iE + u) - D_i\nabla\rho_i \tag{2}$$

$$\nabla \bullet J = 0 \tag{3}$$

$$E = -\nabla\varphi \tag{4}$$

$$k_i = k_{i0}/\delta \tag{5}$$

$$\delta = \frac{PT_0}{P_0T} \tag{6}$$

where φ is the electric potential, ε_0 is the permittivity of free space, ρ_i is the space charge density, J is the current density, E is the electric field strength, k_i is the ion mobility, D_i is the ion diffusion coefficient, u is gas the velocity, δ is the relative gas density ($T_0 = 298.15K$, $P_0 = 101325Pa$), k_{i0} is the ion mobility at the standardized condition (k_{i0}=2.1 × 10^{-4} m^2/V/s).

Typically, the space charge density of particles is much smaller than that of ions [34], so the effect of particle charge is neglected in this study to simplify the calculations.

The electric field strength on the surface of the discharge electrode can be calculated by Peek’s law:

$$E_s = 3.1 \times 10^6 m\delta\left(1 + \frac{0.0308}{\sqrt{\delta r}}\right) \tag{7}$$

where r is the electrode radius.

2.2. Gas flow

The gas flow in an ESP is usually considered viscous, incompressible, steady-state. Thus, the RNG k-ε model was adopted to simulate the flow field within the ESP. The specific equations are as follows:

Conservation of mass:

$$\nabla\left(\rho_{gas}u\right)=0 \tag{8}$$

Conservation of momentum:

$$\rho_{gas}\left(\frac{\partial u}{\partial t}+u\bullet\nabla u\right)=-\nabla P+\mu_{eff}\nabla^2u+\rho_iE \tag{9}$$

where ρ_{gas} is the gas density, μ_{eff} is the effective gas viscosity.

2.3. Particle charging

Particles entering the ESP are charged by two charging mechanisms: diffusion charging and field charging. The integrated charging model proposed by Lawless et al. [35] can calculate the charge during particle motion accurately and is widely used for particle charge calculation:

$$\frac{dq_p}{dt}=\begin{cases}\dfrac{q_s}{\tau}\left(1-\dfrac{q}{q_s}\right)^2+\dfrac{2\pi\alpha\rho_ik_ik_Bd_p}{e} & q\le q_s\\ \dfrac{\alpha}{4\tau}(q-q_s)exp\left(\dfrac{e(q-q_s)}{2\pi\varepsilon_0k_ik_BTd_p}\right) & q>q_s\end{cases} \tag{10}$$

$$\alpha=\begin{cases}1 & e_{norm}<0.525\\ \dfrac{1}{(e_{norm}+0.457)^{0.575}} & e_{norm}>0.525\end{cases} \tag{11}$$

$$e_{norm}=\frac{ed_p}{2k_BT}E \tag{12}$$

$$q_s=3\frac{\varepsilon_r}{\varepsilon_r+2}\pi\varepsilon_0d_p^2E \tag{13}$$

where q_p is the particle charge, q_s is the saturation particle charge, α is the model constant, τ is the time constant, k_B is the Boltzmann constant, e is the electronic charge, d_p is the Particle diameter, e_{norm} is the model constant, ε_r is the relative permittivity of particle.

2.4. Particle migration

In this work, the Lagrangian method was applied to track the motion of charged particles. The motion of dust particles is affected by a variety of forces, but it has been shown that the other forces are negligible compared to the drag force and electric field force. [36]. Therefore, the electric field forces and drag forces were considered primarily in this model. The specific particle migration equation is described as follows:

$$m_p\frac{du_p}{dt}=\frac{1}{8}\pi C_d\rho_{gas}d_p^2|u-u_p|(u-u_p)+Eq_p \tag{14}$$

$$C_d=\begin{cases}\dfrac{24}{Re} & Re<0.1\\ \dfrac{22.73}{Re}+\dfrac{0.0903}{Re^2}+3.69 & 0.1<Re<1\end{cases} \tag{15}$$

$$Re=\frac{\rho_{gas}|u_p-u|d_p}{\mu_{eff}} \tag{16}$$

$$C_c=1+\frac{2\lambda}{d_p}\left(1.257+0.4exp\left(-\frac{1.1d_p}{2\lambda}\right)\right) \tag{17}$$

where Re is the Reynolds number, C_c is the Cunningham correction factor, λ is the mean free path, m_p is the particle mass, u_p is the particle velocity, C_d is the drag coefficient,

The dust collection efficiency of the ESP can be obtained by calculating the equation as follow:

$$\eta=\left(1-\frac{N_{out}}{N_{in}}\right)\times100\% \tag{18}$$

where η is the dust removal efficiency, N_{out} is the amounts of particles at the outlet, N_{in} is the amounts of particles at the inlet.

2.5. Particle adhesion

The trapped particles are attached to the plate by adhesion forces. In this work, the adhesion of particles was simplified by considering only the adhesion between a single particle and the plate. The adhesion force of the charged particle on the plate is mainly composed of two parts: the electrostatic force and non-electrostatic force. Considering the elastic deformation of the particles in contact with the plate, it is reasonable and rigorous to use the pull-off force as the particle non-electrostatic adhesion force in the adhesion model [37].

2.5.1. Pull-off force

JKR model [38] is widely used for the calculation of the pull-off force between the particles and the wall, expressed as follows:

$$F_{po}=\frac{3}{4}\pi W_Ad_p \tag{19}$$

$$\mathrm{a}=\left(F_{po}d_p/2K\right)^{1/3} \tag{20}$$

where W_A is the is the thermodynamic work of adhesion, a is the radius of the contact surface.

Most real surfaces are rough. An analytical expression proposed by Soltani and Ahmadi [39] can accurately predict the pull-off force required to detach particles from a fine roughness surface:

$$F_{po}=\pi a^2Nf_{po}exp\left[-0.6/(\Delta_c)^2\right] \tag{21}$$

where f_{po} is the pull force required to separate the particles from the individual asperity, a is the radius of the contact surface, N is the quantity of asperities per unit contact area. The dimensionless parameter Δ_c is given by:

$$\Delta_c=\delta_c/\sigma \tag{22}$$

where σ represents the standard deviation of the height distribution, δ_c represents the maximum displacement of the asperity tip over its original height before disruption of contact adhesion. δ_c can be expressed as:

$$\delta_c=\left[\frac{f_{po}^2}{3K^2\beta}\right]^{1/3} \tag{23}$$

$$K=\frac{4}{3}\left[\frac{\left(1-\mathrm{v}_1^2\right)}{E_1}+\frac{\left(1-\mathrm{v}_2^2\right)}{E_2}\right]^{-1} \tag{24}$$

where K is the composite Young's modulus, v_i and E_i are the Poisson's ratio and Young's modulus of material i, β is the radius of a single asperity on a rough surface.

σ, β, N satisfy the following equation [40]:

$$\sigma\beta N\simeq0.1 \tag{25}$$

By associating Eqs. (18)–(22) for calculation, the pull-off force between the rough wall and particle can be obtained.

Many industrial particles are not smooth spherical particles but have a bumpy surface. The irregular particle can be approximated as a sphere having a number of bumps as shown in Fig. 1(a). These bumps can be approximated as hemispheres with radius β_0. β_0 can be calculated by the following equation:

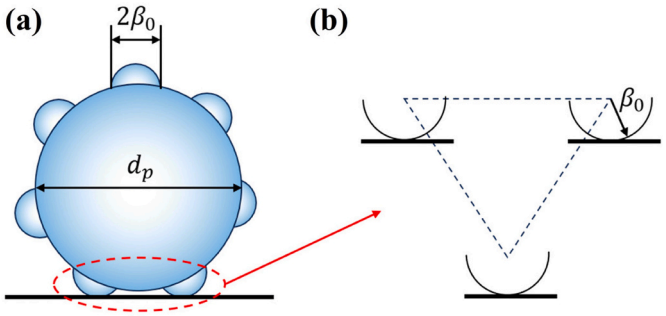

Fig. 1. Schematics of a bumpy particle and contact bumps.

$$\beta_0 = \frac{d_p}{\sqrt{N_0}} \tag{26}$$

where N_0 is the number of bumps on irregular particles.

Typically, irregular particles have three bumps in contact with the wall as shown in Fig. 1(b). So the total pull-off force is calculated as follow:

$$F_{tpo} = 3F_{po} \tag{27}$$

In this work, the pull-off force between the individual bump and the rough wall was first calculated using Eqs. (20)–(25).Then Eq. (26) was used to calculate the total pull-off force. In this work, $\beta = 0.04\beta_0$, $N_0 = 20$, $\sigma = 0.26\mu m$.

2.5.2. Electrostatic force

The charged particles trapped on the plate are subjected to electrostatic adhesion force under the action of electric field, which can be given as [37]:

$$F_e = EQ_p + \frac{Q_p^2}{16\pi\varepsilon_0 y^2} + \frac{Q_p E d_p^3}{16y^3} + \frac{3\pi\varepsilon_0 d_p^6 E^2}{128y^4} \tag{28}$$

where y is the distance from the center of the particle to the wall (for deposited particles, $y = d_p/2$). The terms on the right side of the Eq. (28) are, respectively, the Coulomb force, the image force, the dielectrophoretic force and the polarization force. It is worth noting that the polarization and image forces are always directed towards the collecting plate, whereas the Coulomb and dielectrophoretic forces are affected by the charges they carry and are either both directed towards or away from the plate.

Charged particles deposited onto the pole plate will leak charge to the grounded plate. According to the capacitor principle, the charge of the deposited particles can be expressed by the following equation:

$$Q_p = q_p exp\left(\frac{-t^*}{R\varepsilon_0\varepsilon_r}\right) \tag{29}$$

where R is the resistivity, Q_p is the deposited particle charge , t^* is the time elapsed after the particle reaches the plate.

2.6. Particle re-entrainment

Studies of individual deposited particles have shown that the rupture of the balance between the forces/torques acting on the particles leads to the initial motion of the particles. Therefore, a quasi-static model was employed in this study to simulate the re-entrainment of particles. The quasi-static model focuses only on the inception of particle motion, i.e., the breakdown of the static equilibrium. In this model, resuspension is assumed to occur for each moving particle. The rupture of this static equilibrium can cause three distinct types of initial motion as shown in Fig. 2: sliding, rolling and lift-off [41].

2.6.1. Rolling model

For a particle attached to the plate surface, rolling detachment of the particle will occur when the external torque overcomes the drag torque caused by the total adhesion force, as shown in Fig. 2(a). For small particles in the flow field, in addition to the fluid drag force, the fluid torque also contributes to particle removal. The fluid torque is expressed as [37]:

$$M_h = \frac{2\pi\mu_{eff} f_m d_p^2 u}{C_c} \tag{30}$$

where f_m is the wall correction factor ($f_m = 0.943993$).

The initial condition under which rolling detachment occurs is:

$$M_h + F_d\frac{d_p}{2} \geq F_{AD}0.58\frac{d_p}{\sqrt{N_0}} \tag{31}$$

where F_{AD} is the total adhesion force of the captured charged particles, which consists of the total pull-off force F_{tpo} and electrostatic force F_e. In particle resuspension studies, the minimum critical shear velocity is usually used to characterize the ease with which resuspension of deposited particles can occur [37,42]:

$$u^* = \sqrt{\frac{2u_c\upsilon}{\gamma d_p}} \tag{32}$$

where u_c represents the flow velocity at the particle center when rolling occurs, γ represents the turbulence burst strength factor ($\gamma \sim 1.74$), υ represents the gas kinematic viscosity. In the calculation process, u_c was first obtained by solving Eq. (31), and then the critical shear velocity u^* was computed by solving Eq. (32).

2.6.2. Sliding model

If the friction force is smaller than external force paralleling the plate, the particles will be detached by sliding [37]:

$$F_d \geq k\left(F_e + F_{tpo}\right) \tag{33}$$

where k is surface friction coefficient ($k = 0.2$).

Similarly, the critical shear velocity u^* that causes the particles to slide can be calculated according to Eqs. (32) and (33).

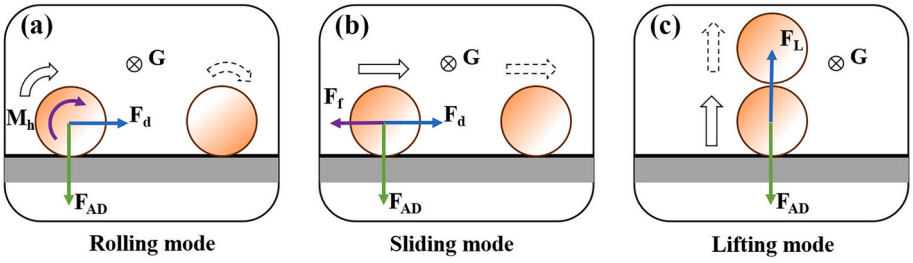

Fig. 2. Three types of single-particle entrainment.

2.6.3. Lift-off model

For uncharged particles, the particle detachment from the surface is mainly triggered by particle motion along the surface (rolling and sliding), as the lifting force plays a negligible role. However, for charged particles in an ESP, the electrostatic force may become the lifting force that makes the particles rise. Thus, the particles will be detached by lifting if:

$$F_e \geq F_{AD} \tag{34}$$

2.7. ESP model parameters and numerical procedures

2.7.1. Structural parameters of the computational domain

In this work, the two-dimensional wire-plate ESP structure was used as the computational domain. The specific geometric parameters are shown in Fig. 3. The length of the collecting plate was 0.8 m. This ESP was equipped with three corona electrodes, each having a diameter of 2 mm. These electrodes were evenly spaced at a distance of 0.2 m from each other. The distance between the collecting plate and corona electrode was 0.1 m. The meshing of the model was performed using a free triangular mesh in the COMSOL Multiphysics, and a refined mesh was applied around the electrodes, thus improving the convergence and accuracy of the computations. Mesh sensitivity analysis was performed during simulation to guarantee the accuracy and efficiency of the simulated outcomes.

2.7.2. Operating parameters

A variety of physical property parameters were involved in this model. Here, the gaskinetic viscosity and density at different temperatures were directly adopted from the air physical parameters in the material library of COMSOL Multiphysics. The resistivity of pyrolyzed coal particles at different temperatures was measured by a high-temperature particle resistivity meter, and the measured experimental value (Table 1) was used as the particle resistivity in the model. The rest of the physical property parameters are listed in Table 2.

2.7.3. Boundary condition

The boundary conditions of the model are presented in Table 3.

2.7.4. Numerical procedure

The simulation executed the following procedures: First, the computational domain and boundary conditions were initialized. Secondly, the electric field and flow field models were coupled and calculated to ascertain the flow field and electric field characteristics. The source term of the control equation was automatically updated according to the calculation results, and the surface's calculated electric field strength on the discharge electrode was compared with that calculated by Peek's formula to determine whether it converges or not. Then the particle injection took place within the computational domain, and the particle transport characteristics were obtained by solving the particle charging and migration equation. Finally, the adhesion and re-entrainment characteristics of the particles deposited on the plate were obtained by solving the particle adhesion and re-entrainment model.

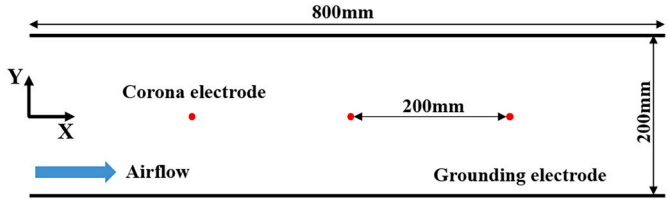

Fig. 3. Structure of the ESP.

Table 1
Particle resistivity at different temperatures.

Temperature (°C)	200	400	600
Resistivity, R (Ω·cm)	5.28×10^8	2.08×10^7	6.11×10^5

Table 2
Main operating conditions and parameter.

Parameter (unit)	Value	Parameter (unit)	Value
Temperature, T (°C)	200–600	Inlet velocity, u_{in} (m/s)	0.4–1.2
Pressure, P (atm)	1	Particle permittivity, ε_r	5
Particle density, ρ_p (kg/m^3)	2200	Particle diameter, d_p (μm)	1–10
Particle Young's modulus, E_1 (GPa)	94	Particle Poisson's ratio, ν_1	0.16
Plate Young's modulus, E_2 (GPa)	191	Plate Poisson's ratio, ν_2	0.3

Table 3
Boundary conditions for the ESP model.

Position	Particle	Gas flow	Space charge	Electric field
Inlet	Velocity	Velocity	$\frac{\partial \rho_i}{\partial n} = 0$	$\frac{\partial \varphi}{\partial n} = 0$
Outlet	Disappear	Pressure	$\frac{\partial \rho_i}{\partial n} = 0$	$\frac{\partial \varphi}{\partial n} = 0$
Corona electrode	Bounce back	Non-slip	Peek formula	$\varphi = U$
Grounding electrode	Freeze	Non-slip	$\frac{\partial \rho_i}{\partial n} = 0$	$\varphi = 0$

3. Results and discussion

3.1. Model validation

To authenticate the precision of the simulation outcomes, the simulation results of discharge characteristics, flow field, collection efficiency and particle adhesion were compared with the previous experimental results [43–46], as shown in Fig. 4. The simulation details and experimental data sources are shown in Table 4. Experimental data of discharge characteristics, flow field and collection efficiencies were measured from ESP systems with different configurations. The adhesion force of charged particles was measured by Mizes [46] using the atomic force microscopy (AFM) technique. From the figure, it is evident that the simulation results remarkably coincide with the experimental results. Therefore, the present model is verified to be accurate and can be used for further studies.

3.2. The ESP performance at different temperatures

3.2.1. The corona field at different temperatures

To thoroughly examine the impact of temperature on the ESP performance, we conducted a comparative analysis of the electric field and space charge distribution across three distinct temperatures (200 °C, 400 °C, and 600 °C) while maintaining a constant operating voltage of 40 kV. Fig. 5 illustrates the variations in electric field and space charge distribution within the ESP at these temperatures. As can be seen from Fig. 5(a)(c), the regions with high electric field and high space charge density predominantly localize near the discharge electrode. Besides, a corona shielding region characterized by low electric field and low charge emerges between adjacent electrodes, resulting from the mutual inhibition between adjacent discharge electrodes. Fig. 5(b) demonstrates that temperature differentially affects the electric field strength near the discharge electrode and the collection plate when the voltage remains constant. Near the discharge electrode, the electric field strength is diminished at elevated temperatures, whereas it marginally increases near the collection plate as temperature rises. Nonetheless, the influence of temperature on overall electric field strength is relatively

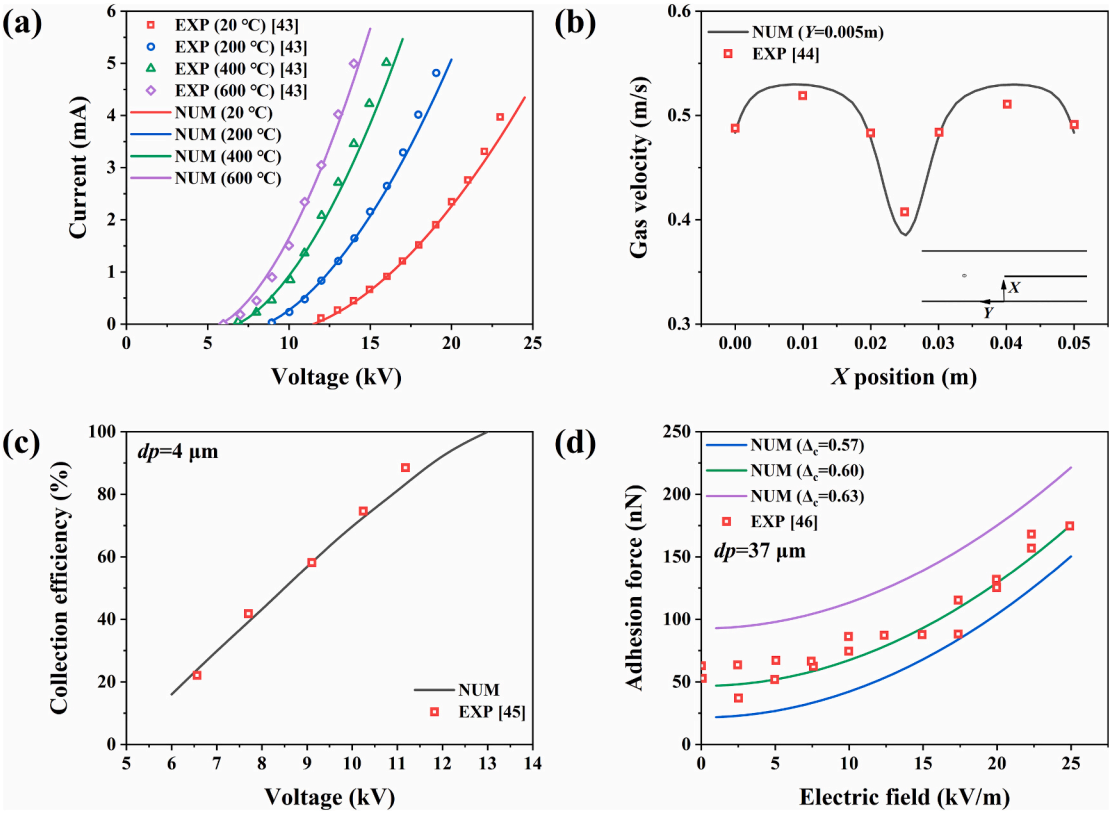

Fig. 4. Comparison between simulated and experimental values: (a) corona current [43], (b) flow field [44], (c) collection efficiency [45], (d) adhesion force [46].

insignificant, constrained by the constant applied voltage. In contrast to its slight impact on electric field strength, temperature exerts a more pronounced effect on space charge density, as depicted in Fig. 5(d). With rising temperatures, there is a marked increase in space charge density across the entire dusting space.

3.2.2. *The flow field at different temperatures*

Particle re-entrainment due to airflow scour is a significant factor affecting the ESP efficiency, necessitating thorough investigation into the flow field distribution within the ESP. In our model, we employed wall function to approximate the surface conditions of the ESP plates, omitting the viscous sublayer of turbulent boundary layers. Therefore, the computed flow velocity at the plate surface (Y = 0.1 m) could actually provide an indication of the flow dynamics in the immediate vicinity of the plate. The electrohydrodynamic (EHD) flow in the ESP is formed by the coupling of the main flow and ionic wind. Fig. 6(a) illustrate the variations in flow field distribution with and without the inclusion of the ionic wind, at an inlet flow velocity of 0.4 m/s, with solid black lines representing the flow streamlines. It can be observed that the ionic wind produced an extremely violent disturbance of the main flow. This effect results in the formation of two pairs of distinct vortex structures in the ESP: one situated on the plate surface upstream of the discharge electrode, and the other at the channel center downstream of the discharge electrode. These vortices significantly disrupt the spatial uniformity of the flow field by compressing the main flow and creating regions of increased velocity within the ESP. Observing the streamlines reveals that the airflow is deflected towards the collection plate after traversing the discharge electrode, with a concomitant acceleration in flow velocity. On the one hand, this deflection and acceleration facilitate particle migration to the collection plate, thereby enhancing particle capture, but on the other hand, it also intensifies the direct airflow scouring to the collection plate surface, potentially leading particle re-entrainment. Fig. 6(b) shows the near-plate flow velocity in the ESP before and after considering the ionic wind. The dotted line represents the discharge electrode position. It is observed that the ionic wind led to a region of high velocity near the plate, which predominantly situated between the adjacent discharge electrodes and at the outlet. At an inlet flow rate of only 0.4 m/s, the flow velocity close to the plate surface can reach a maximum of 1.01 m/s. Such a zone of high velocity may induce rigorous airflow scouring over the dust layer, potentially undermining the stability of the accumulated particles and prompting re-entrainment.

Fig. 7 illustrates the distributions of the flow field and the near-plate flow velocity at varying temperatures. The inlet flow velocity was 0.8 m/s, and the applied voltage was 40 kV. As can be seen from the Fig. 7(a), an increase in temperature from 200 °C to 600 °C results in a progressive intensification of the vortex within the flow field, exerting a greater compressive effect on the main flow and thereby increasing the unevenness of the flow field. Moreover, the airflow traversing the discharge electrode exhibits an increased deflection towards the collection plate accompanied by an elevated flow velocity at elevated temperatures. This phenomenon can be attributed to the enhancement of the ionic wind effect at higher temperatures. As shown in Section 3.2.1, at the same voltage, the high temperatures yield a stronger electric field near the plate and increased space charge density over the total dusting space, thus generating a more forceful ionic wind. Fig. 7(b) shows the near-plate flow velocity in the ESP at different temperatures. The peak near-plate flow velocity increased with increasing temperature. Illustratively, in the high-velocity region situated between the first and second discharge electrodes, the peak flow velocity ascends from 0.75 m/s to 1 m/s as temperature increases from 200 °C to 600 °C. This trend suggests that elevated temperatures foster the development of local high-velocity zones in the ESP's near-plate region, potentially leading to particle re-entrainment.

The above flow field distributions are all the calculation results for the ESP with circular wire discharge electrodes. In industrial applications, to improve the collection efficiency, discharge electrodes of increased discharge intensity and intricate geometries, such as needle

Table 4
Simulation details for verification of the model.

Fig.	Properties	Value	Experimental data sources
(a)	ESP structure	Wire-cylinder	[43]
	Discharge electrode number	1	
	Discharge electrode diameter (mm)	0.5	
	Grounding tube diameter (mm)	80	
	Discharge electrode length (mm)	1680	
	Temperature (°C)	20, 200, 400, 600	
	Pressure (atm)	1	
(b)	ESP structure	Wire-plate (two-stage)	[44]
	Discharge electrode number	1	
	Discharge electrode diameter (mm)	0.22	
	Pre-charger length (mm)	100	
	Collection stage length (mm)	100	
	ESP width (mm)	50	
	Inlet flow velocity (m/s)	0.5	
	Voltage on the discharge electrode (kV)	10	
	Voltage of the collection stage (kV)	5	
	Temperature (°C)	25	
	Pressure (atm)	1	
(c)	ESP structure	Wire-plate	[45]
	ESP length (mm)	400	
	ESP width (mm)	50	
	Discharge electrode number	8	
	Discharge electrode diameter (mm)	0.1	
	Discharge electrode spacing (mm)	50	
	Temperature (°C)	25	
	Pressure (atm)	1	
	Inlet flow velocity (m/s)	2	
	Particle permittivity	2.5	
	Particle diameter (μm)	4	
	Particle density (kg/m^3)	894	
(d)	Particle diameter (μm)	8.3	[46]
	Particle Young's modulus (GPa)	69	
	Particle Poisson's ratio	0.2	
	Plate Young's modulus (GPa)	69	
	Plate Poisson's ratio	0.33	

electrodes and arista electrodes, are frequently employed. Fig. 8 contrasts the flow field associated with a circular-wire electrode and that of a needle electrode. As shown in Fig. 8(a), the flow field in the needle-electrode ESP exhibits greater unevenness compared to that in the circular-wire-electrode ESP. This disparity is attributed to the strong ionic wind effect generated by the high discharge intensity of the needle electrode. In the needle-electrode ESP, the enhanced ionic wind causes a more significant deflection of the main flow downstream of the discharge electrodes towards the collection plate, accompanied by increased flow velocity, implying a more vigorous airflow scouring effect. Fig. 8(b) presents the flow velocity distribution in the near-plate zone of the circular-wire-electrode and needle-electrode ESPs. The needled-electrode ESP demonstrates a higher peak near-plate velocity. Specifically, the peak velocity between the first and second discharge electrodes is 0.88 m/s for the circular wire electrode, whereas it escalates to 1.8 m/s with the needle electrode. Consequently, using electrodes with complex shapes, such as needle electrodes, in high-temperature ESPs may cause more intense particle re-entrainment.

3.2.3. Particle re-entrainment

To comprehensively describe the re-entrainment of deposited particles in the ESP, a large number of particles were uniformly injected into the ESP in the model. After the particles were trapped, the dynamics of the deposited particles across the collection plate was analyzed.

In an ESP, charged particles in a turbulent flow field were attached on the collection plate due to electrostatic and pull-off forces. This section first compared the contribution of these two forces in particle adhesion. Fig. 9 shows comparative evaluation of the average electrostatic force and the pull-off force acting on particles with varying diameters when they are just trapped (t^*=0 s). The dashed line shows the variation of the average pull-off force with particle diameter for different values of the dimensionless roughness parameter, Δ_c. The findings indicate an increase in both adhesive forces with particle size. Furthermore, the pull-off force decreases as the Δ_c decreases. For any given value of Δ_c, a specific critical diameter exists. Electrostatic force is dominant for particles with a diameter larger than it, but for particles with a diameter smaller than it, pull-off forces dominate. In this study, we focus on particles mainly influenced by electrostatic forces. Consequently, for subsequent calculations, we have selected a smaller value for Δ_c, specifically $\Delta_c = 0.3$, unless mentioned otherwise.

Critical shear velocity u^* is a key parameter for characterizing the resuspension of particles. A higher u^* suggests that a greater fluid velocity is necessary to resuspend particles, indicating more resistance to resuspension [37]. The critical shear velocities predicted by the sliding and rolling models for particles with different diameters (1, 3, 5, 7 μm) at the initial time (t^*=0) are shown in Fig. 10. It is observed that the critical shear velocity exhibits an undulating distribution with the particle position (X). The critical shear velocity is lower at the inlet and outlet. Moreover, the peak of the critical shear velocity occurs near the X value corresponding to the discharge electrode, and the valley occurs between the two discharge electrodes. This can be contributed to the variation in adhesion forces experienced by particles at different locations on the collection plate. Specifically, the area near the discharge electrode, characterized by a strong electric field and high space charge density, subjects particles to high electrostatic adhesion forces. Conversely, regions positioned between adjacent discharge electrodes as well as those near the inlet and outlet, where the electric field strength and charge density diminish, exhibit reduced electrostatic adhesion forces acting on particles. Especially for particles trapped near the entrance, which, due to short charging time, possess lesser charges and consequently experience lower critical shear velocities. Combined with the results of Section 3.2.2, it can be seen that most of the particles with low critical shear velocities are located in the high velocity regions of the flow field—namely, regions between adjacent discharge electrodes and at the inlet and outlet. These observations suggest a greater propensity for particle re-entrainment in these specific areas during the operation of an ESP. Fig. 10 also shows that the critical shear velocity decreases with increasing particle size, indicating that lager particles are more susceptible to re-entrainment. Furthermore, a comparison between Fig. 10 (a) and (b) reveals that the critical shear velocity of rolling detachment is lower than that of sliding detachment, suggesting a higher likelihood of particle re-entrainment through rolling.

Deposited particles on the collection plate, continuously charged by the corona electric field, also gradually release charge to the collection plate over time. This release of charge can potentially reduce the electrostatic adhesion of the particles. The critical shear velocities for the re-entrainment of 5-μm particles within 6 μs after reaching the collection plate at different temperatures are shown in Fig. 11. When the particles are just captured to the collection plate (t^*=0), the critical shear velocities of rolling and sliding detachment increase with increasing temperature. This trend is attributed to the increased space charge density and electric field in the near-plate region of the ESP due to elevated temperatures under the constant voltage, which contribute to an increased electrostatic force acting on deposited particles at the initial moment (t^*=0). Over time, both rolling and sliding critical shear velocities tend to decrease. The rate of this decrease is more pronounced at higher temperatures. At a high temperature of 600 °C, the critical

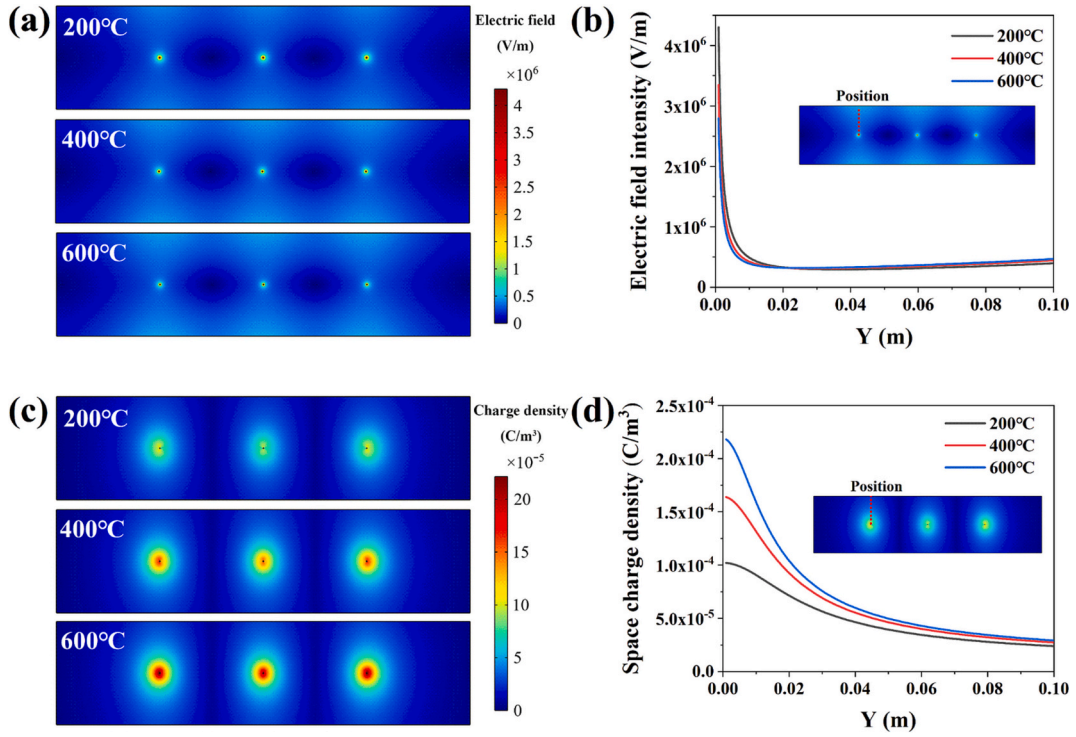

Fig. 5. The electric field at different temperatures: (a) 2-D plot, (b) 1-D plot. The space charge density at different temperatures: (c) 2-D plot, (d) 1-D plot.

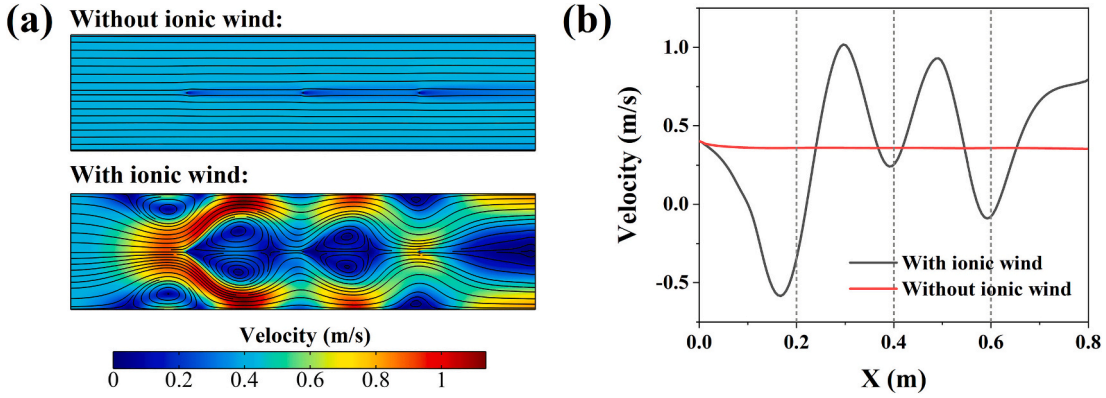

Fig. 6. The flow field with and without ionic wind: (a) 2-D plot, (b) line distribution of the velocity in the near-plate region (T= 400 °C, u_{in}=0.4 m/s, U= 40 kV).

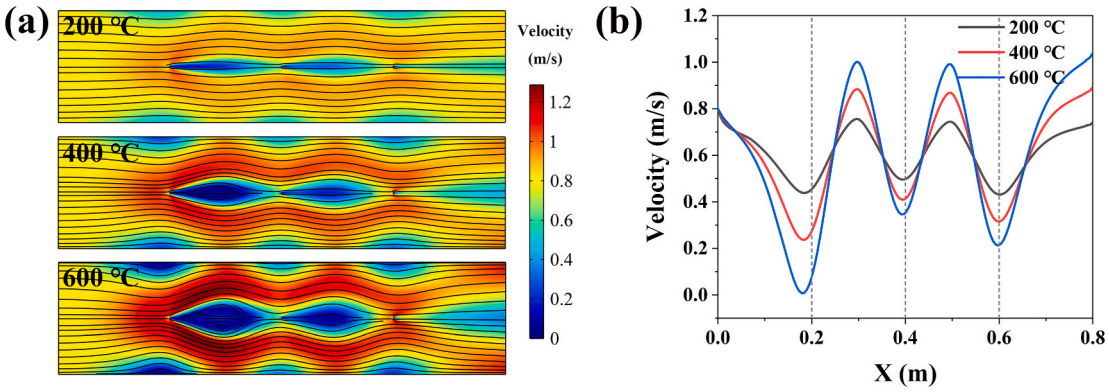

Fig. 7. The flow field at different temperatures: (a) 2-D plot, (b) line distribution of the velocity in the near-plate region (u_{in}=0.8 m/s, U=40 kV).

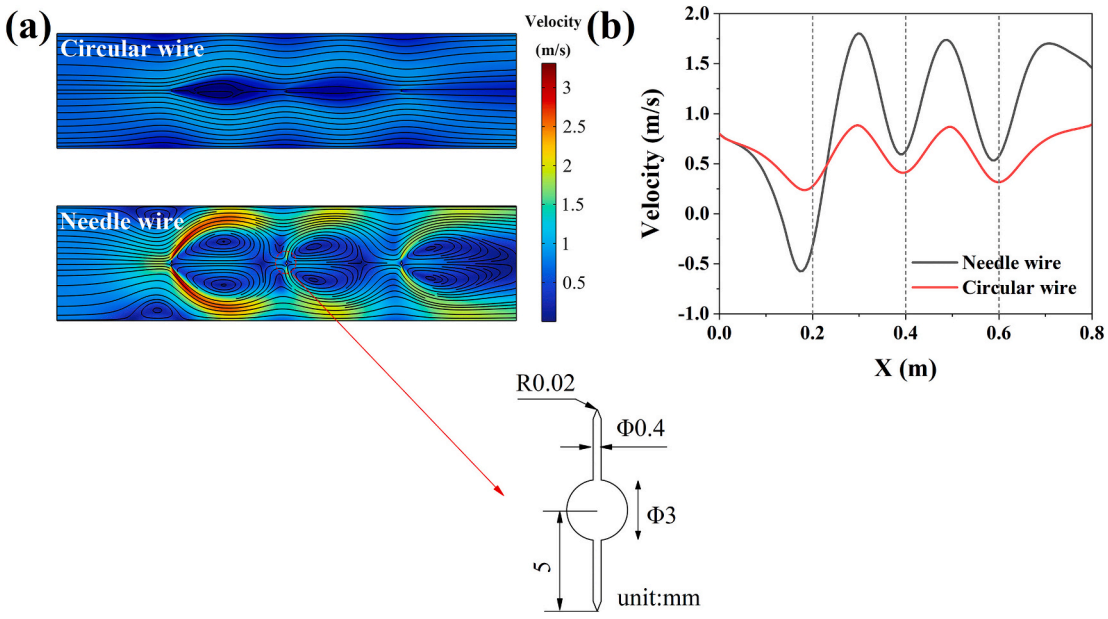

Fig. 8. Comparison of flow field between circular wire electrode and needle wire electrode ESPs: (a) 2-D plot, (b) line distribution of the velocity in the near-plate region (T= 400 °C, u_{in}=0.8 m/s, U= 40 kV).

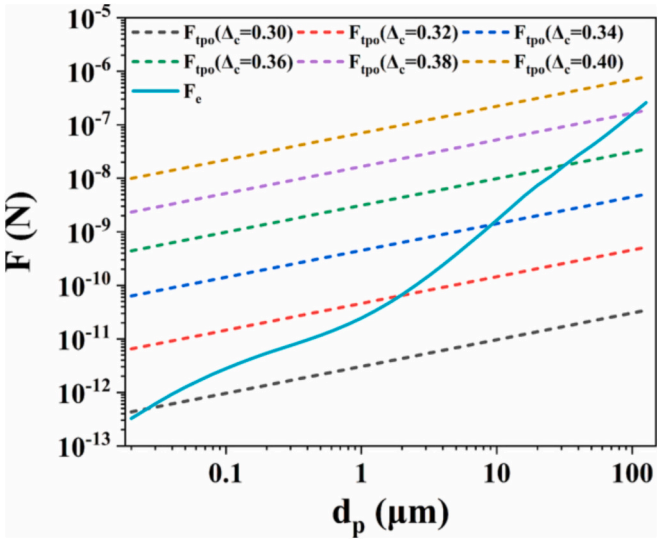

Fig. 9. Variations of the electrostatic and pull-off forces with the diameter (T= 400 °C, u_{in}=1.2 m/s, U= 40 kV).

shear velocity experiences a notably rapid decline as time progresses. Taking the temporal variation of the maximum critical shear velocity for sliding and rolling detachment at different temperatures (Fig. 12) as an example. The maximum critical shear velocities for sliding and rolling detachment decrease from 1.27 m/s and 0.95 m/s to 0.35 m/s and 0.26 m/s, a reduction of 72.4% and 72.6%, respectively, after particles are trapped on the collection plate for just 6 μs at 600 °C. This means that particle re-entrainment intensifies at elevated temperatures, due to the accelerated decrease in critical shear velocity. It is attributed to the low resistivity of the particles at high temperatures (Table 1) which results in rapid particle charge release and a subsequent decrease in electrostatic adherence.

Notably, for high-temperature particles trapped in the high-velocity region, resuspension occurs rapidly due to the large reduction in critical shear velocity. However, if these particles are situated in the low-velocity region, where the fluid forces are inadequate to counteract the adhesion forces, the particles will likely maintain adherence to the collection plate. In this case, due to the substantial release of particle charge within a brief period, eventually the particles will acquire induced charges of opposite polarity, and thus be detached by lifting under the action of electrostatic lifting force, as shown in Fig. 13(a). The induced charge could be calculated by [47]:

$$Q_i = 1.65\pi\varepsilon_0 d_p^2 E \tag{35}$$

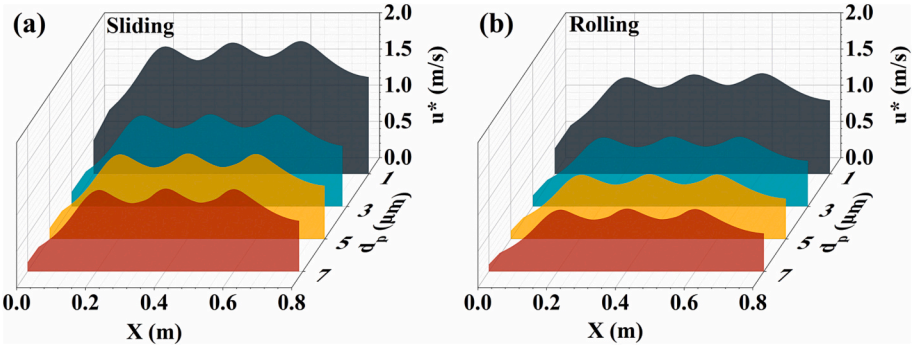

Fig. 10. Critical shear velocities for re-entrainment of particles with different diameters by (a) sliding and (b) rolling (T= 400 °C, u_{in}=1.2 m/s, U= 40 kV).

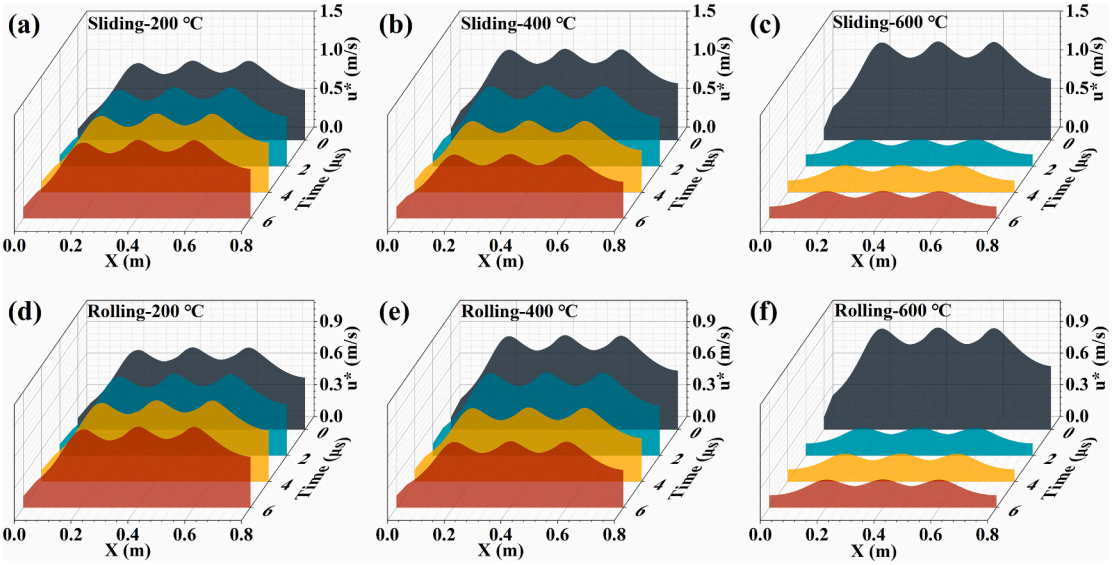

Fig. 11. Variation of critical shear velocity with time for (a), (b), (c) sliding and (d), (e), (f) rolling detachment of 5-μm particles at different temperatures (u_{in}=1.2 m/s, U= 40 kV).

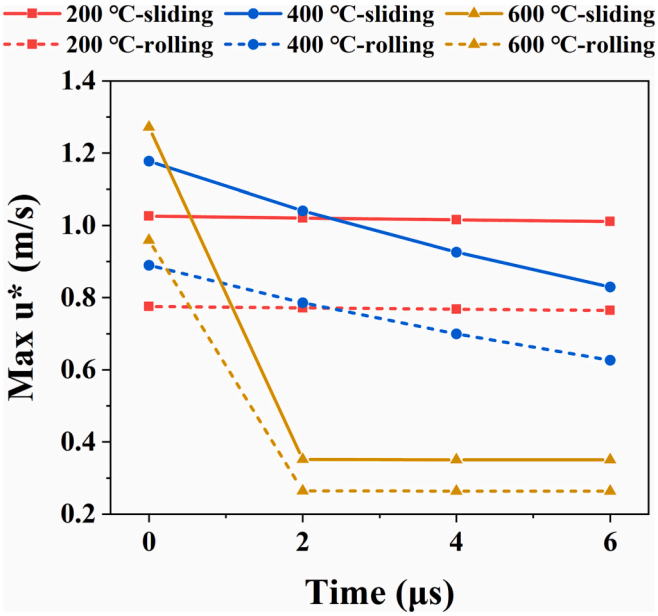

Fig. 12. Variation of maximum critical shear velocity with time at different temperatures (u_{in}= 1.2 m/s, U= 40 kV).

Fig. 13(b) illustrates the average induced electrostatic force and the average pull-off force for particles with different diameters at 600 °C. It is observed that the electrostatic lifting force increased with increasing particle diameter. Furthermore, large particles are more likely to be resuspended by lifting detachment under electrostatic lifting force than small particles.

3.3. Countermeasures against particle re-entrainment

As mentioned above, two prominent causes result in the intensified re-entrainment of particles at high temperature: 1. At a constant voltage, the ion wind effect is enhanced at high temperature, which makes the unevenness of the flow field increase, and the near-wall region prone to the existence of high-velocity area, thus exacerbating the particle re-entrainment caused by the airflow scouring; 2. Due to the lower particle resistivity at high temperatures, the deposited particles rapidly release charges or even attach induced charges of opposite polarity, which reduces the adhesion between the particles and the collection plate, making the particles easier to be detached by sliding, rolling or lifting. Consequently, it is essential for high-temperature ESP to reduce particle re-entrainment. Many methods have been proposed by researchers to inhibit particle re-entrainment, e.g., two-stage ESPs [48], electrostatic flocking technology [49,50], etc. Currently, the most common method to inhibit particle re-entrainment is by optimizing the structure of the collection plate. Numerous studies have been conducted on traditional collection plates with complex shapes (e.g., C-type plates, corrugated-type plates, etc.) [51,52], and in recent years some new collection plates (e.g., hole-type plates [32,53–56]) have been proposed as potentially better collection plates to reduce particle re-entrainment. This section investigates five distinct collection plate geometries to assess their impact on particle re-entrainment. The structures of collection plate evaluated include flat-type, C-type, corrugated-type, W-type, and hole-type plates. The specific geometrical parameters of each plate are shown in Fig.S1. Here, the inlet flow velocity is 1.2 m/s, the applied voltage is 30 kV, and the temperature is 400 °C.

3.3.1. Characteristics of flow field

In this section, the flow field of ESPs with different collection plates were compared, as shown in Fig. 14. It is observed that collection plates with complex structures have an improved effect on the space flow field. Except for the flat-type collection plate, all other plate types exhibit varying degrees of low-velocity regions in the near-wall region. Among them, the hole-type and corrugated-type plates have more extensive low-velocity regions, whereas the regions associated with C- and W-type plates are comparatively smaller. Fig. 14(f) illustrates the average flow velocities in the near-wall region of the ESP with different collection plates. The average flow velocities in the near-wall region of the plates with complex structures are all significantly lower compared to the flat-type plate. Among them, the corrugated-type plate demonstrates the lowest average flow velocity in the near-wall region, followed by the C-type and hole-type plate. And the W-type plate exhibits higher flow velocity in the near-wall region than the other three. From the above analyses, it can be seen that using plates with complex structure in an ESP can generate a beneficial low-velocity region near the plate, which can effectively reduce particle re-entrainment caused by airflow scouring and minimizes particle escape during practical operations.

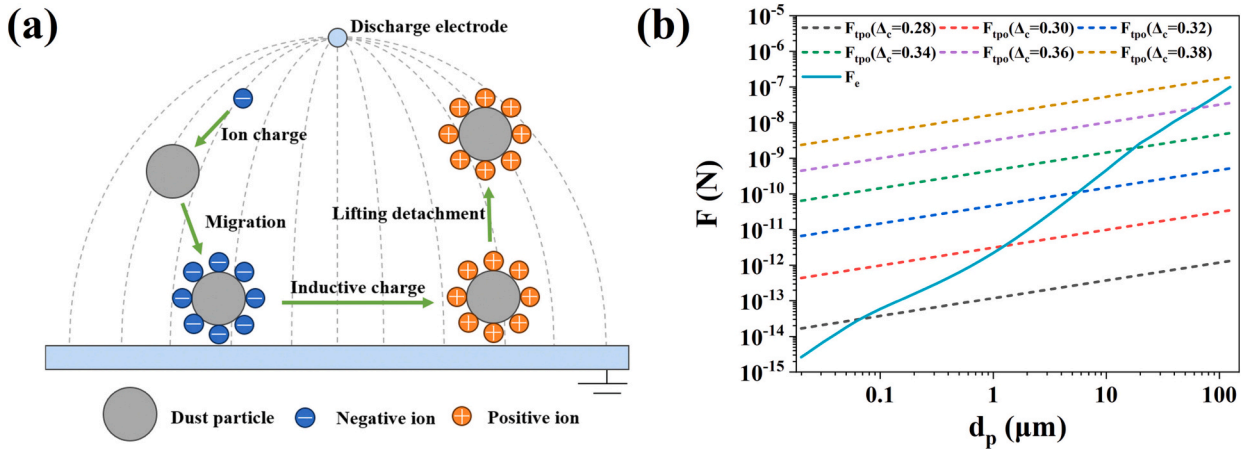

Fig. 13. (a) Mechanism of charged particle lift detachment. (b) Comparison of electrostatic lifting forces and pull-off forces on particles of different diameters (T=400 °C, u_{in}=1.2 m/s, U= 40 kV).

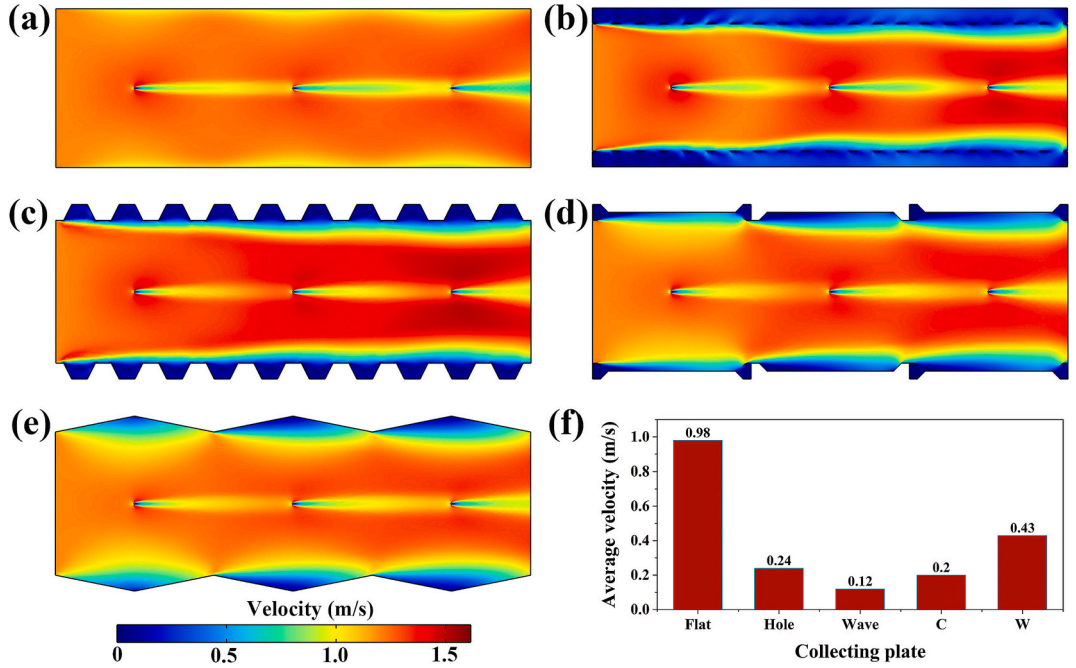

Fig. 14. Flow field distribution in the ESP with different collection electrodes. (a) Flat type. (b) Hole type. (c) Wave type. (d) C type. (e) W type. (f) Comparison of near-plate average flow velocities.

Moreover, among the four complex collection plates examined, corrugated-type and hole-type plates appear more effective at curbing particle re-entrainment, while W-type plate is relatively less effective in suppressing particle re-entrainment.

3.3.2. *Characteristics of electric field*

Fig. 15 illustrates the electric field distribution of the ESP with various configurations of collection plates. As the figure shows, the structure of the collection plate has a negligible impact on the electric field distribution in the vicinity of the discharge electrode. Note that the electric field strength between the discharge electrode and the perforated guidance plate in the hole-type ESP is higher than that in other ESPs. This is because the presence of the perforated plate is equivalent to shortening the distance between the discharge electrode and the grounding electrode, thus making the electric field strength between them increase. The structure of the collection plate significantly influences the electric field strength adjacent to it. A low electric field region occurs in the area near the complex collection plates, especially for the hole-type plate. In a hole-type ESP, the perforated guide plate acts as an electrical shield, leading to an extensive area with a low electric field between the guide plate and grounding electrode. Compared to the hole-type plate, the other types of collection plates have smaller low electric field regions. The weakened field regions for corrugated-type and C-type plates are predominantly located within the grooves of these plates, whereas the W-type plate does not exhibit a marked low electric field region. Fig. 15(f) gives the average electric field strength at the plate surface for different collection plates. Here, the dark-colored columns represent the average electric field at the total plate surface and the light-colored columns represent the average electric field at the plate surface in the low electric field region. The total plate-averaged electric field strengths of the complex collection plates are all smaller than those of the flat-type plate, with the hole-type plate having the smallest total plate-averaged electric field strengths. The C-type plate has the smallest plate-averaged electric field strength of low

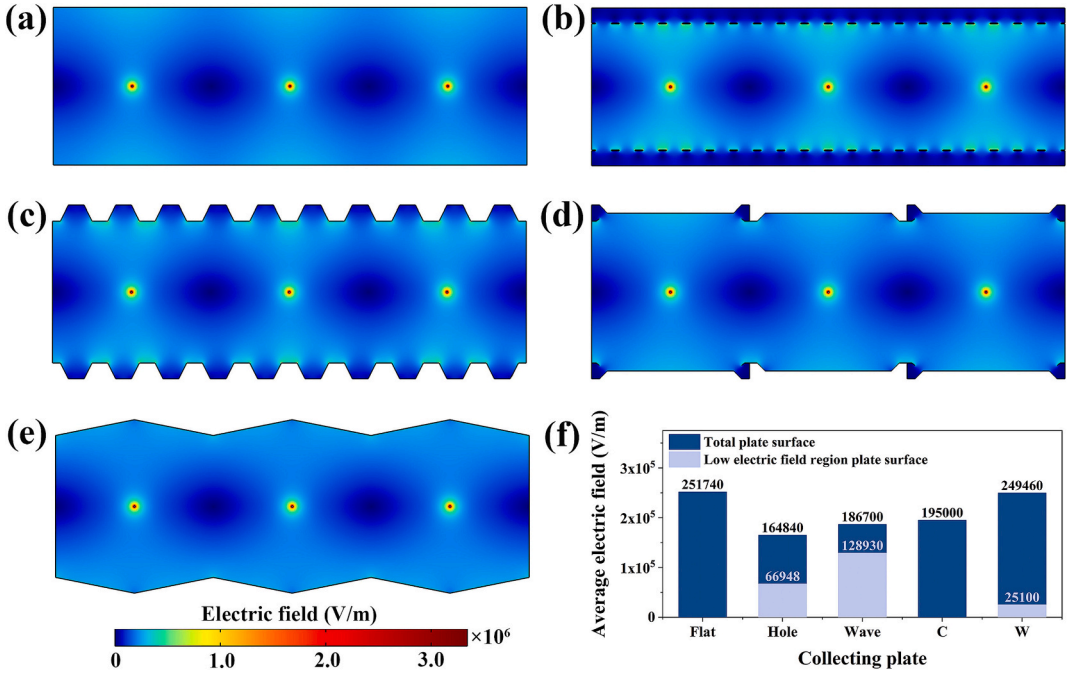

Fig. 15. Electric field distribution in the ESP with different collection electrodes. (a) Flat type. (b) Hole type. (c) Wave type. (d) C type. (e) W type. (f) Comparison of plate-averaged electric field strengths.

electric field region; however, its low electric field region is very narrow relative to that of corrugated-type and hole-type plates, being confined only to the grooves at the ends of the plate. Consequently, this results in a relatively high total plate-averaged electric field for the C-type plate, surpassed only by that of the flat-type plate. According to Section 3.2.3, for high-temperature ESP, in addition to particle re-entrainment due to airflow scouring, high-temperature particles may acquire induced charges of opposite polarity due to low resistivity, and thus be re-entrained by electrostatic lifting. Hence, a weaker electric field on the plate surface can effectively reduce particle detachment due to electrostatic lifting at high temperatures. Additionally, the low electric field region near the plate surface can also prevent the occurrence of sparks within the dust layer, thereby diminishing particle re-entrainment due to spark breakdown between stacked particles [32]. Based on the above analyses, the hole-type ESP, with its more expansive low electric field regions and lower plate-averaged electric field, may provide superior performance in reducing particle re-entrainment caused by electrostatic lifting and spark breakdown.

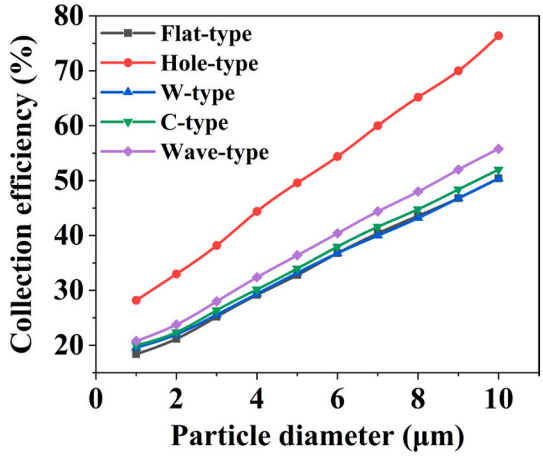

Fig. 16. Collection efficiency in the ESP with different collection electrodes.

3.3.3. *Comparison of collection efficiency*

Fig. 16 shows a comparison of the collection efficiency of ESPs with different collection plates. It can be found that the collection efficiency of the ESP with hole-type plate is significantly higher than that of the ESP with other collection plates. This can be explained by the high electric field strength between the perforated guide plate and the discharge electrode (as shown in Section 3.3.2). In general, elevated electric field strength can enhance the electric field force acting on the particles thus promoting particle deposition.

The design of high temperature ESP collection plates requires consideration of various factors, particularly the effect on breakdown voltage. The reduction in breakdown voltage at elevated temperatures critically impairs the performance of high-temperature ESPs. Notably, the findings presented in Fig. 16 are obtained with the same voltage applied. It can be expected that different collection plates will inevitably influence the breakdown voltage of the ESP thus affecting the maximum collection efficiency. This suggests the necessity for further experimental research to ascertain the precise effects of differing plate designs on both the breakdown voltage and the peak collection efficiency.

Despite this, prior analyses of flow fields and electric fields indicates that the hole-type ESP is capable of reducing the particle re-entrainment caused by airflow scouring and electrostatic lifting at high temperatures by generating a zone characterized by low velocity and low electric field between the perforated guide plate and the grounding plate. Therefore, adopting a hole-type collection plate may be a better potential method to reduce particle re-entrainment in high-temperature ESPs.

4. Conclusions

In this work, an integrated model was developed to investigate the flow field distribution and high-temperature particle re-entrainment effects in the high-temperature ESPs. The following conclusions can be drawn:

Ionic wind causes significant disturbances to the flow field within ESPs, increasing the unevenness of that field and leading to the formation of local high-velocity regions near plate surfaces, which may induce particle re-entrainment. Under the constant voltage, an increase in temperature will intensify the ionic wind effect, exacerbate the

unevenness of the flow field, and raise the peak velocity in the high-velocity regions near the plate, thereby increasing the likelihood of particle re-entrainment. Compared to circular wire electrodes, the use of needle wire electrodes in ESPs results in a more uneven flow field and higher peak velocities near the plate, leading to greater particle re-entrainment potential.

Deposited particles adhere to the plate due to electrostatic and pull forces. There exists a critical shear velocity, beyond which particles detached by sliding, rolling, or lifting. The critical shear velocities required for particles to slide or roll off show a wavy distribution depending with the deposited particles position, with valley value typically occurring at the inlet and outlet as well as between adjacent discharge electrodes, indicating a higher probability of particle re-entrainment at these locations. The critical shear velocity of the particles decreases over time due to the charge release. Elevated temperatures further accelerate this decline, making particles more susceptible to be re-entrained at high temperatures. Additionally, high-temperature particles that are not blown away by airflow may eventually attach induced charges of opposite polarity and then be detached from the plate by lifting under electrostatic forces.

Based on these findings, the effectiveness of five types of collection plates in suppressing particle re-entrainment effects was compared. Among them, the hole-type plate is able to generate a region with low velocity and low electric field near the plate, effectively controlling the particle re-entrainment caused by both airflow scouring and electrostatic lifting. This indicates its potential superiority in minimizing particle re-entrainment in high-temperature ESPs.

CRediT authorship contribution statement

Yongmin Shi: Writing – original draft, Methodology, Investigation, Conceptualization. **Chao Li:** Supervision, Project administration. **Mengxiang Fang:** Writing – review & editing, Resources, Funding acquisition. **Jianmeng Cen:** Validation, Data curation. **Qinhui Wang:** Supervision. **Keping Yan:** Validation, Supervision.

Declaration of competing interest

The authors declare that they have no known competing financial interests or personal relationships that could have appeared to influence the work reported in this paper.

Data availability

Data will be made available on request.

Acknowledgments

This work was supported by the Fundamental Research Funds for the Central Universities (2022ZFJH004) and National Key R&D Program of China (2018YFB0605000).

Appendix A. Supplementary data

Supplementary data to this article can be found online at https://doi.org/10.1016/j.powtec.2024.119538.

References

[1] G. Ahmadi, D.H. Smith, Gas flow and particle deposition in the hot-gas filter vessel of the Pinon pine project, Powder Technol. 128 (2002) 1–10.
[2] T. Melchior, R. Madlener, Economic evaluation of IGCC plants with hot gas cleaning, Appl. Energy 97 (2012) 170–184.
[3] G. Xiao, X. Wang, J. Zhang, M. Ni, X. Gao, Z. Luo, K. Cen, Granular bed filter: a promising technology for hot gas clean-up, Powder Technol. 244 (2013) 93–99.
[4] S.D. Sharma, M. Dolan, D. Park, L. Morpeth, A. Ilyushechkin, K. McLennan, D. J. Harris, K.V. Thambimuthu, A critical review of syngas cleaning technologies — fundamental limitations and practical problems, Powder Technol. 180 (2008) 115–121.
[5] M. Lupion, M. Rodriguez-Galan, B. Alonso-Fariñas, F.J. Gutierrez Ortiz, Investigation into the parameters of influence on dust cake porosity in hot gas filtration, Powder Technol. 264 (2014) 592–598.
[6] I.A. El-Hedok, L. Whitmer, R.C. Brown, The influence of granular flow rate on the performance of a moving bed granular filter, Powder Technol. 214 (2011) 69–76.
[7] G. Rinard, D.E. Rugg, T. Yamamoto, High-temperature high-pressure electrostatic precipitator electrical characterization and collection efficiency, IEEE T Ind. Appl. IA-23 (1987) 114–119.
[8] A. Jaworek, A. Krupa, T. Czech, Modern electrostatic devices and methods for exhaust gas cleaning: a brief review, J. Electrost. 65 (2007) 133–155.
[9] M. Ni, X. Wang, G. Xiao, K. Qiu, G. Yang, X. Gao, K. Cen, Development of back corona discharge in a wire-cylinder electrostatic precipitator at high temperatures, Powder Technol. 286 (2015) 789–797.
[10] J.B. Thomas, E. Wong, Experimental study of dc Corona at high temperatures and pressures, J. Appl. Phys. 29 (1958) 1226–1230.
[11] J.R. Bush, P.L. Feldman, M. Robinson, High temperature, high pressure electrostatic precipitation, J. Air Pollut. Control Assoc. 29 (1979) 365–371.
[12] G. Xiao, X. Wang, G. Yang, M. Ni, X. Gao, K. Cen, An experimental investigation of electrostatic precipitation in a wire–cylinder configuration at high temperatures, Powder Technol. 269 (2015) 166–177.
[13] G. Xiao, X. Wang, J. Zhang, M. Ni, X. Gao, K. Cen, Characteristics of DC discharge in a wire-cylinder configuration at high ambient temperatures, J. Electrost. 72 (2014) 13–21.
[14] P. Bürger, U. Riebel, High temperature coronas in air and flue gas from LPG combustion: current-voltage characteristics, ion mobilities and free electrons, J. Electrost. 115 (2022) 103676.
[15] P. Bürger, U. Riebel, Feasibility of high-temperature electrostatic precipitation for the removal of nanoparticles: a case study on iron oxide separation at up to 800 °C, J. Electrost. 120 (2022) 103754.
[16] X. Xu, X. Gao, P. Yan, W. Zhu, C. Zheng, Y. Wang, Z. Luo, K. Cen, Particle migration and collection in a high-temperature electrostatic precipitator, Sep. Purif. Technol. 143 (2015) 184–191.
[17] P. Yan, C. Zheng, G. Xiao, X. Xu, X. Gao, Z. Luo, K. Cen, Characteristics of negative DC corona discharge in a wire–plate configuration at high temperatures, Sep. Purif. Technol. 139 (2015) 5–13.
[18] P. Bürger, U. Riebel, Formation of highly resistive SiO2 nanoparticle layers from the aerosol by electrostatic precipitation at 200 °C: observations on back corona and nanoparticle layer structure, J. Nanopart. Res. 23 (2021).
[19] X. Xu, C. Zheng, P. Yan, W. Zhu, Y. Wang, X. Gao, Z. Luo, M. Ni, K. Cen, Effect of electrode configuration on particle collection in a high-temperature electrostatic precipitator, Sep. Purif. Technol. 166 (2016) 157–163.
[20] Q. Chen, M. Fang, J. Cen, Y. Zhao, Q. Wang, Y. Wang, Electrostatic precipitation under coal pyrolysis gas at high temperatures, Powder Technol. 362 (2020) 1–10.
[21] T. Wen, I. Krichtafovitch, A.V. Mamishev, Numerical study of electrostatic precipitators with novel particle-trapping mechanism, J. Aerosol Sci. 95 (2016) 95–103.
[22] C. Zheng, C. Liang, S. Liu, Z. Yang, Z. Shen, Y. Guo, Y. Zhang, X. Gao, Balance and stability between particle collection and re-entrainment inawide temperature-range electrostatic precipitator, Powder Technol. 340 (2018) 543–552.
[23] J. Podlinski, A. Niewulis, J. Mizeraczyk, P. Atten, ESP performance for various dust densities, J. Electrost. 66 (2008) 246–253.
[24] J. Podliński, A. Niewulis, J. Mizeraczyk, Electrohydrodynamic flow and particle collection efficiency of a spike-plate type electrostatic precipitator, J. Electrost. 67 (2009) 99–104.
[25] Z. Ning, J. Podlinski, X. Shen, S. Li, S. Wang, P. Han, K. Yan, Electrode geometry optimization in wire-plate electrostatic precipitator and its impact on collection efficiency, J. Electrost. 80 (2016) 76–84.
[26] D. Yan, Z. Zhang, H. Gong, Y. Ya, Effect of barbed tubular electrode corona discharge EHD flow on submicron particle collection in a wide-type ESP, J. Electrost. 109 (2021) 103545.
[27] A. Krupa, J. Podliński, J. Mizeraczyk, A. Jaworek, Velocity field of EHD flow during back corona discharge in electrostatic precipitator, Powder Technol. 344 (2019) 475–486.
[28] Z. Yuan, K. Yanagawa, Y. Ehara, Visualization and analysis of a re-entrained particle with an electrostatic precipitator using PIV method, J. Electrost. 119 (2022) 103751.
[29] K. Adamiak, Numerical models in simulating wire-plate electrostatic precipitators: a review, J. Electrost. 71 (2013) 673–680.
[30] G. Lee, S. Hwang, T. Cheon, H. Kim, B. Han, S. Yook, Optimization of pipe-and-spike discharge electrode shape for improving electrostatic precipitator collection efficiency, Powder Technol. 379 (2021) 241–250.
[31] Y. Zhu, M. Gao, M. Chen, J. Shi, W. Shangguan, Numerical simulation of capture process of fine particles in electrostatic precipitators under consideration of electrohydrodynamics flow, Powder Technol. 354 (2019) 653–675.
[32] Y. Wang, W. Gao, H. Zhang, Z. Yang, Z. Zhao, L. Shao, Z. Sun, C. Zheng, X. Gao, Significance of ionic wind propulsion on charged particle removal during flue gas purification, Powder Technol. 410 (2022) 117804.
[33] Y. Zhu, Z. Wei, X. Yang, S. Tao, Y. Zhang, W. Shangguan, Comprehensive control of PM 2.5 capture and ozone emission in two-stage electrostatic precipitators, Sci. Total Environ. 858 (2023) 159900.
[34] Z. Yang, C. Zheng, S. Liu, Y. Guo, C. Liang, X. Zhang, Y. Zhang, X. Gao, Insights into the role of particle space charge effects in particle precipitation processes in electrostatic precipitator, Powder Technol. 339 (2018) 606–614.

[35] P.A. Lawless, Particle charging bounds, symmetry relations, and an analytic charging rate model for the continuum regime, J. Aerosol Sci. 27 (1996) 191–215.
[36] K. Luo, Y. Li, C. Zheng, X. Gao, J. Fan, Numerical simulation of temperature effect on particles behavior via electrostatic precipitators, Appl. Therm. Eng. 88 (2015) 127–139.
[37] M. Soltani, G. Ahmadi, Detachment of rough particles with electrostatic attraction from surfaces in turbulent flows, J. Adhes. Sci. Technol. 13 (1999) 325–355.
[38] K.L. Johnson, K. Kendall, A.D. Roberts, Surface energy and the contact of elastic solids, Proc.R.Soc.Lond.A 324 (1971) 301–313.
[39] M. Soltani, G. Ahmadi, R.G. Bayer, M.A. Gaynes, Particle detachment mechanisms from rough surfaces under substrate acceleration, J. Adhes. Sci. Technol. 9 (1995) 453–473.
[40] J.A. Greenwood, J.B.P. Williamson, Contact of nominally flat surfaces, Proc.R.Soc. Lond.A 295 (1966) 300–319.
[41] C. Henry, J. Minier, S. Brambilla, Particle resuspension: challenges and perspectives for future models, Phys. Rep. 1007 (2023) 1–98.
[42] B. Nasr, G. Ahmadi, A.R. Ferro, S. Dhaniyala, A model for particle removal from surfaces with large-scale roughness in turbulent flows, Aerosol Sci. Technol. 54 (2020) 291–303.
[43] U. Riebel, C. Lübbert, S. Lebedynskyy, Elektroabscheider - es gibt noch viel zu tun, CHEM-ING-TECH 84 (2012) 1099–1113.
[44] M. Gao, Y. Zhu, X. Yao, J. Shi, W. Shangguan, Dust removal performance of two-stage electrostatic precipitators and its influencing factors, Powder Technol. 348 (2019) 13–23.
[45] K.D. Kihm, Effects of Nonuniformities on Particle Transport in Electrostatic, Stanford University, 1987.
[46] H.A. Mizes, Adhesion of small particles in electric fields, J. Adhes. Sci. Technol. 8 (1994) 937–951.
[47] A.Y.H. Cho, Contact charging of micron-sized particles in intense electric fields, J. Appl. Phys. 35 (1964) 2561–2564.
[48] A. Zukeran, Y. Ikeda, Y. Ehara, M. Matsuyama, T. Ito, T. Takahashi, H. Kawakami, T. Takamatsu, Two-stage-type electrostatic precipitator re-entrainment phenomena under diesel flue gases, IEEE T Ind. Appl. 35 (1999) 346–351.
[49] A. Niewulis, J. Podliński, M. Kocik, R. Barbucha, J. Mizeraczyk, A. Mizuno, EHD flow measured by 3D PIV in a narrow electrostatic precipitator with longitudinal-to-flow wire electrode and smooth or flocking grounded plane electrode, J. Electrost. 65 (2007) 728–734.
[50] B.J. Sung, A. Aly, S.H. Lee, K. Takashima, S. Kastura, A. Mizuno, Fine-particle collection using an electrostatic precipitator equipped with an electrostatic flocking filter as the collecting electrode, Plasma Process. Polym. 3 (2006) 661–667.
[51] W. Zhou, R. Jiang, Y. Sun, B. Chen, B. Liu, Study on multi-physical field characteristics of electrostatic precipitator with different collecting electrodes, Powder Technol. 381 (2021) 412–420.
[52] W. Gao, Y. Wang, H. Zhang, B. Guo, C. Zheng, J. Guo, X. Gao, A. Yu, Numerical simulation of particle migration in electrostatic precipitator with different electrode configurations, Powder Technol. 361 (2020) 238–247.
[53] H. Kawakami, A. Zukeran, K. Yasumoto, T. Inui, T. Yamamoto, Numerical simulation of three-dimensional particle migration and electrohydrodynamics of double cylinder electrostatic precipitator, Int. J. Plasma Environ. Sci. Technol. 6 (2012) 104–110.
[54] Y. Ehara, M. Ohashi, A. Zukeran, K. Kawakami, Y. Aoki, Development of hole-type electrostatic precipitator, Int. J. Plasma Environ. Sci. Technol. 11 (2017) 9–12.
[55] H. Kawakami, A. Zukeran, K. Yasumoto, T. Yamamoto, Diesel PM collection for marine emissions using double cylinder type electrostatic precipitator, Int. J. Plasma Environ. Sci. Technol. 5 (2011) 174–178.
[56] H. Kawakami, A. Zukeran, K. Yasumoto, T. Inui, T. Yamamoto, Numerical simulation of re-entrained particle migration for double cylinder type electrostatic precipitator, Mar. Eng. 46 (2011) 769–776.